Chapter 3

Reinvestigating atomic ordering in $K_{0.5}Na_{0.5}NbO_3$ and its impact on ferroelectric properties

3.1 Introduction

The structure-property correlations in perovskite-based oxides with ABO_3 type structures lead to a diverse range of applications *viz.*, non-linear photonics, sensors, energy harvesters, ultrasonic transducers, optical wave guides, infrared and terahertz generation & detection and many more [36, 71, 97, 172, 214, 215, 216, 217, 218, 219, 220]. Lead-based perovskites such as $PbZr_{1\text{-}x}Ti_xO_3$ (PZT) [114, 221, 222, 223, 224], (1-x)$Pb(Mg_{1/3}Nb_{2/3})O_3$-$x$$PbTiO_3$ (PMN-xPT) [47, 222, 224], and (1-x)$Pb(Zn_{1/3}Nb_{2/3})O_3$-$x$$PbTiO_3$ (PZN-xPT) [47, 222, 224] excel in wide range of applications. Owing to toxic nature of lead [225, 226], alternatives like Potassium Sodium Niobate ($K_xNa_{(1\text{-}x)}NbO_3$; KNN$x$) and other alkali niobates are being explored [153, 161, 162]. Here, KNNx is a solid solution of ferroelectric $KNbO_3$ and antiferroelectric $NaNbO_3$. $KNbO_3$ and $NaNbO_3$ have orthorhombic symmetry with $Amm2$ ($1a_p \times \sqrt{2}b_p \times \sqrt{2}c_p$) and $Pbcm$ ($\sqrt{2}a_p \times \sqrt{2}b_p \times 4c_p$) space groups respectively

[8, 27, 160, 163]. The increasing potassium content (x) in $NaNbO_3$ leads to the modification in the unit cell *via* octahedral rotation, octahedral distortions, and(or) cationic displacements. This, in turn, results in the suppression/disappearance of the intensity corresponding to the superlattice reflection(s) and(or) splitting of the main perovskite reflections, by the reduction in the size of the supercell (*i.e.*, antiferrodistortive phase transition) and the distortion of the subcell/elementary cell (*i.e.*, ferrodistortive phase transition) respectively. The orthorhombic phase of $NaNbO_3$ (Space Group: *Pbcm*) with compound tilt system $(a^-a^-c^+)_1^2(a^-a^-c^-)_2^3(a^-a^-c^+)_3^4$ transforms into a monoclinic phase with simple tilt system *Pm* $(a^-b^+c^-)$ for $0.02 \leq x \leq 0.15$. On increasing potassium content (x), the tilts start vanishing, giving rise to monoclinic phases with different tilt systems *viz.*, *Pm* $(a^-b^+c^0)$ and *Pm* $(a^0b^+c^0)$ stable for compositions (x) namely $0.17 \leq x \leq 0.30$, and $0.35 \leq x \leq 0.45$ respectively [164, 165]. Owing to the morphotropic phase boundary observed for the equimolar composition of $KNbO_3$ and $NaNbO_3$ namely $x = 0.50$ (KNN50), KNN50 has always been in discussion for extremum in various physical properties [115, 169]. Different authors have reported tilt free monoclinic phase *Pm* [56, 115] and an orthorhombic phase *Amm*2 [55, 115, 167, 170] for KNN50 using various characterization techniques *viz.*, Raman scattering, X-ray diffraction, Synchrotron X-ray diffraction, neutron diffraction, and electron diffraction. Orayech *et al*. analyzed the long-range atomic ordering of KNN50 as a function of temperature using X-ray and neutron diffraction data [55]. A series of structures were found to be stable *viz.*, *R*3*c* (T < 135 K), *Amm*2 (135 K < T < 465 K), *P*4*mm* (465 K < T < 700 K), and $Pm\bar{3}m$ (T > 700 K) [55]. Moreover, Kong *et al*. analyzed the neutron diffraction data of KNN50 and reported the structure to be monoclinic (*Pm*), which is stable down to 100 K [56]. Further, ferrodistortive phase transitions from monoclinic (*Pm*) to tetragonal (*P*4*mm*) and finally to cubic ($Pm\bar{3}m$) have been reported at T $\approx$ 471 K and 674 K, respectively [56]. In addition, Kong *et al.* and

Gupta *et al.* analyzed the short-range structure of KNN50 using Pair Distribution Function (PDF) data and found the atomic ordering to be monoclinic with *Pm* space group [56, 171].

Various ferrodistortive phase transitions of KNN50 are driven by component(s) freezing of the soft phonon mode(s) corresponding to the zone center ($q = 0,0,0$) of the cubic Brillouin zone [55, 227]. Among various soft phonon mode(s) associated with the Γ-point of the cubic Brillouin zone, Γ_4^- is responsible for ferroelectric ordering [104, 227]. The component freezing of Γ_4^- phonon mode along three dimensions gives different crystal symmetry with ferroelectric displacements. Various crystal symmetries namely tetragonal (*P*4*mm*), orthorhombic (*Amm*2), and rhombohedral (*R*3*m*) are obtained when the ferroelectric phonon mode Γ_4^- freezes along one, two, and three dimensions with equal magnitude(s) resulting in order parameter direction (OPD) $(a,0,0)$, $(a,a,0)$, and (a,a,a) respectively. Further, monoclinic (*Pm*), monoclinic (*Cm*), and triclinic (*P*1) symmetries result from the freezing along two and three dimensions with unequal magnitudes leading to OPD's $(a,b,0)$, (a,a,b), and (a,b,c) respectively [89].

The ferrodistortive phases can be observed at both the long and short ranges, which are responsible for ferroelectric properties. The long-range crystal structure is obtained from Bragg scattering [228, 229, 230, 231], while the short-range structure is obtained from the diffuse scattering, which is either too weak or gets lost during background subtraction [211]. Thus, a total scattering method, including Bragg and diffuse scattering, is implemented to address both the long and short-range atomic ordering existing in the crystalline material. The Pair Distribution Function (PDF) is the most prominent technique, which includes total scattering to probe the atomic scale structure *i.e.*, short-range ordering [211]. The main principle behind the technique involves X-ray diffraction data whose Fourier transform gives the distribution of atomic pair distances existing in the material [208]. Thus, X-ray diffraction and PDF analysis provide the complete structural information of a material.

In the present thesis work, we have explored the structure-property relationship near MPB region of KNNx ceramics (x = 0.40, 0.50, and 0.60). Traditional X-ray diffraction combined with Rietveld analysis has been utilized to study long-range ordering (LRO) in the crystals, while pair distribution function data has been analyzed using PDFGUI software to study short-range ordering (SRO) in the crystals. Moreover, Raman scattering data has also been used to determine the atomic ordering of KNNx ceramics. Further, an innovative frozen phonon mode approach has been used in order to get an insight of ferroelectric distortions leading to high ferroelectric (or polarization) properties in the vicinity of widely reported MPB composition KNN50.

3.2 Experimental procedure

The $K_xNa_{(1\text{-}x)}NbO_3$ (KNNx) ceramics were prepared *via* conventional solid-state reaction route with raw chemicals *viz.*, K_2CO_3 (99%) (Sisco Research Laboratories Pvt. Ltd.) (99%), Na_2CO_3 (99%) (HIMIDEA Labs) (99.5%), and Nb_2O_5 (99%) (HIMIDEA Labs) (99.9%) dried at 393 K prior to weighing. The dried raw chemicals were weighed accordingly followed by milling for 24 hours. The milled powder was further calcined at 1123 K. The calcined powder is mixed with 2-5 % PVA binder and was pelletized at 7-8 metric tons pressure. The pellets were further sintered at temperature of 1323 K for 4h. The X-ray diffraction measurement was carried out by Rigaku Smart Lab high-resolution X-ray diffractometer with Cu-Kα1(λ=1.54059 Å) radiation. The room temperature Raman spectra of KNNx ceramics has been collected over a wide spectral range of 80 cm^{-1} to 1000 cm^{-1} using the alpha300 RAS system from WITec with an excitation source of 532 nm green laser.

The high energy (λ = 0.1173 Å) synchrotron X-ray diffraction data (SXRD) for atomic structure calculations were obtained from the beam line at Argonne National Laboratory. The obtained dataset was then reduced to structure function $S(Q)$ given as follows [208, 211]:

$$S(Q) = 1 + \frac{[I_{\text{coh}}(Q) - \Sigma c_i |f_i(Q)|^2]}{|\Sigma f_i(Q) c_i|^2} \tag{3.1}$$

where, Q is the wavevector ($Q = 4\pi sin\theta/\lambda$) with 2θ being the angle between incoming and outgoing X-rays, $I_{\text{coh}}(Q)$ is the coherent part of diffraction data, c_i and $f_i(Q)$ are the atomic concentrations and X-ray structure factor of atomic species of i^{th} type. The S(Q) obtained from high energy synchrotron source at Argonne National Lab, Chicago have been taken over broad range of Q with S(Q) finally converging to 1 at large Q. Further, the Fourier transform of S(Q) was done with Q_{max} = 28 Å^{-1} in order to obtain the final pair distribution function G(r) [208, 211]:

$$G(r) = \frac{2}{\pi} \int_{Q_{\text{min}}}^{Q_{\text{max}}} Q[S(Q) - 1] sin(Qr) dQ \tag{3.2}$$

Further, the decomposition of frozen phonon modes have been studied using AMPLIMODES [232, 233] software available at Bilbao Crystallographic Server [234, 235].

3.3 Results and discussions

3.3.1 Long Range Order in KNN*x*

The X-ray profiles for KNN*x* (0.40, 0.50, and 0.60) ceramics are plotted in Fig. 3.1, showing the formation of single phase with insets representing the main perovskite reflections *viz.*, {200}, {220}, and {222}. The reported structures for KNN*x* ceramics in the vicinity of MPB composition (*i.e.*, KNN50) are orthorhombic (Space Group: *Amm*2) [55, 167], and monoclinic (Space Group: *Pm*) [56]. In order to resolve the ambiguity regarding the crystallographic structure of KNN50 (orthorhombic (*Amm*2) [55, 167] and/or monoclinic (*Pm*) [56]) and its nearby compositions, we have considered the splitting of main perovskite reflections resulting from the distortions of the ideal perovskite.

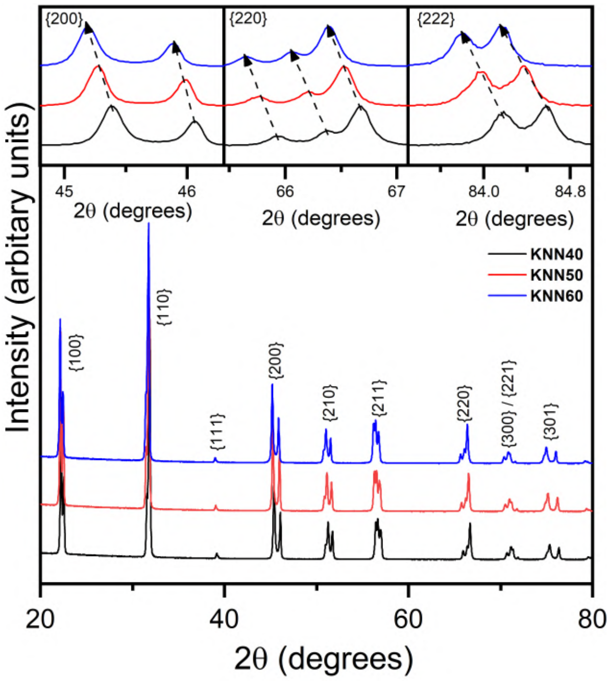

Fig. 3.1 X-ray diffraction peaks evolution of KNNx (x = 0.40, 0.50, and 0.60) ceramics with insets showing the evolution of the main perovskite peaks *viz*., {200}, {220}, and {222} of KNNx ceramics.

Now, for an orthorhombic unit cell with one formula unit per unit cell *i.e*., *Pmm*2 and bigger orthorhombic unit cell (orthorhombic in rhombic orientation) with two formula units per unit cell *i.e*., *Amm*2, the {h00}, {hh0}, and {hhh} type reflections corresponding to the cubic symmetry splits into 3, 3, and 1 reflection for *Pmm*2 and 2, 3, and 2 reflections for *Amm*2. The difference in the number of reflections for the two orthorhombic unit cells with different formula units is reminiscent of a different symmetry at the elementary level ($1a_p \times 1b_p \times 1c_p$) for bigger orthorhombic unit cell (*Amm*2). The different symmetry for *Amm*2 at the elementary level is consistent with a constrained monoclinic cell *i.e*., pseudo-monoclinic ($a_p \neq b_p = c_p$; $\alpha_p \neq 90^o$, $\beta_p = \gamma_p = 90^o$). The bigger orthorhombic unit cell (*Amm*2) is related to the elementary pseudo-monoclinic cell as follows [227, 236, 237]:

$$a_\mathrm{p} = A_0 \tag{3.3}$$

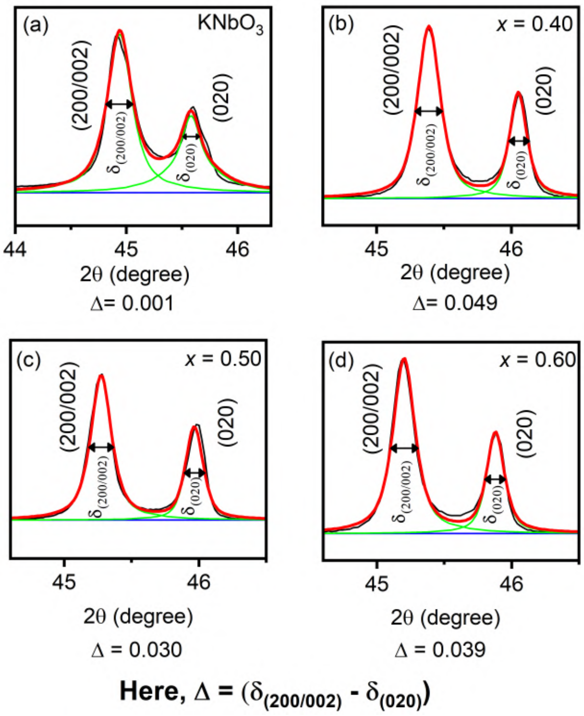

Fig. 3.2 Fitted profiles of {200} reflections of KNNx ceramics depicting FWHM differerence (Δ=$\delta_{(200)/(002)}$-$\delta_{(020)}$) for (a) KNbO$_3$, (b) $x = 0.40$ (KNN40), (c) $x = 0.50$ (KNN50), and (d) $x = 0.60$ (KNN60) ceramics.

$$b_p = c_p = \frac{1}{2}(\sqrt{B_0^2 + C_0^2}) \tag{3.4}$$

$$B_0^2 = b_p^2 + c_p^2 - 2b_pc_pcos(\alpha_p) \tag{3.5}$$

$$C_0^2 = b_p^2 + c_p^2 + 2b_pc_pcos(\alpha_p) \tag{3.6}$$

and with a constraint b_p=c_p we get pseudo-monoclinic angle (α_p),

$$sin(\frac{\alpha_p}{2}) = \frac{B_0}{2b_p} \tag{3.7}$$

where A_0, B_0, and C_0 are lattice parameters of the bigger orthorhombic unit cell, while a_p, b_p, and c_p are the lattice parameters of the elementary pseudo-monoclinic cell [227, 236, 237].

Now, in the peak profiles of HR-XRD patterns of KNN*x* ceramics we observe 2, 3, and 2 reflections visible for {h00}, {hh0}, and {hhh} family of planes (see insets of Fig. 3.1). The two reflections corresponding to {hhh} family of planes rules out the possibility of orthorhombic unit cell having one formula unit per unit cell (*i.e*, *Pmm*2) suggesting the structure can be either orthorhombic with two formula units per unit cell (*i.e*, *Amm*2 having different symmetry at elementary level) or monoclinic (*Pm*). For orthorhombic unit cell (*Amm*2) we observe 2, 3, and 2 reflections, while for monoclinic (*Pm*) cell we observe 3, 4, and 2 reflections corresponding to {h00}, {hh0}, and {hhh} family of planes. Here, in between *Pm* and *Amm*2, the major difference sets in for {h00} family of planes [115, 238]. The additional broadening observed for the monoclinic (*Pm*) cell arrives from partial overlapping of (h00) and (00h) peaks, while for orthorhombic unit cell (*Amm*2), (h00) and (00h) peaks overlap completely. This is examined by calculating full width at half maxima (FWHM) ($\delta_{\{h00\}} = 2\theta_1 - 2\theta_2$) for {h00} family of planes (see Fig. 3.2). The FWHM difference (Δ) between (200)/(002) and (020) reflections is given as:

$$\Delta = \delta_{\{200\}/\{002\}} - \delta_{\{020\}} \tag{3.8}$$

The FWHM difference (Δ) is found to be significant ($\approx 0.030°$ *i.e.*, $\delta_{\{200\}/\{002\}} > \delta_{\{020\}}$) for KNN50 (see Fig. 3.2(c)) suggesting the unit cell to be monoclinically distorted [115, 238]. On the other hand, the FWHM difference (Δ) for pure $KNbO_3$ is zero when indexed with orthorhombic unit cell using *Amm*2 space group (see Fig. 3.2(a)) [115]. Moreover, the FWHM difference for all the compositions comes out to be significantly greater than zero, suggesting monoclinic symmetry for KNN*x* (x = 0.40, 0.50, and 0.60) ceramics (see Fig. 3.2).

Further, to confirm the monoclinic symmetry (Space Group: *Pm*), Rietveld refinements were carried out for KNN*x* ceramics (x = 0.40, 0.50, and 0.60) using FULLPROF package [239]. In the refinements, isotropic thermal parameters for K/Na, Nb, and O were refined

Table 3.1 Various structural parameters, and agreement factors obtained from the Rietveld (LRO) and PDF (SRO) refinements of the X-ray diffraction patterns and PDF profile for x = 0.40 *via* monoclinic (*Pm*) model at LRO and SRO respectively.

	Rietveld Refinement				PDF Refinement			
	Space group: *Pm*				Space group: *Pm*			
Atoms	x	y	z	$B_{\text{iso}}(\text{Å}^2)$	x	y	z	$U_{\text{equiv}}(\text{Å}^2)$
K/Na	0.0164(8)	0.0000	0.0237(15)	0.5940(29)	0.9774(110)	0.0000	0.0364(210)	0.0113(15)
Nb	0.4834(6)	0.5000	0.5296(8)	0.2290(4)	0.4726(90)	0.5000	0.5082(120)	0.0043(14)
O_1	0.5238(26)	0.5000	0.0166(37)	1.2270(124)	0.4727(310)	0.5000	0.0271(210)	0.0162(177)
O_2	-0.0157(38)	0.5000	0.4968(25)	0.5980(113)	0.0296(100)	0.5000	0.4832(200)	0.0171(120)
O_3	0.5106(24)	0.0000	0.4894(20)	0.4930(97)	0.5852(310)	0.0000	0.4730(340)	0.0152(164)
	a=3.988(1)Å, b=3.937(3)Å, c=3.992(1)Å,				a=4.033(14)Å, b=3.937(15)Å, c=3.948(14)Å,			
	β=90.322(1)				β=91.161(153)			
	V=62.669(2)Å^3				V=62.667(20)Å^3			
	Agreement factors: R_{wp}=7.54, R_{exp}=6.04, χ^2=5.38				Agreement factors: R_w=11.49%			

Table 3.2 Various structural parameters, and agreement factors obtained from the Rietveld (LRO) and PDF (SRO) refinements of the X-ray diffraction patterns and PDF profile for x = 0.50 *via* monoclinic (*Pm*) model at LRO and SRO respectively.

	Rietveld Refinement				PDF Refinement			
	Space group: *Pm*				Space group: *Pm*			
Atoms	x	y	z	$B_{\text{iso}}(\text{Å}^2)$	x	y	z	$U_{\text{equiv}}(\text{Å}^2)$
K/Na	0.0742(50)	0.0000	0.0773(49)	1.2080(33)	0.9713(350)	0.0000	0.0347(170)	0.0145(100)
Nb	0.5578(22)	0.5000	0.5837(19)	0.2240(11)	0.4722(120)	0.5000	0.5106(120)	0.0043(12)
O_1	0.6068(34)	0.5000	0.0166(28)	0.0600(106)	0.5226(240)	0.5000	0.0094(270)	0.0179(45)
O_2	0.0338(54)	0.5000	0.5555(32)	0.0300(184)	0.0284(200)	0.5000	0.4882(510)	0.0158(130)
O_3	0.5980(60)	0.0000	0.5457(49)	0.0656(200)	0.5937(370)	0.0000	0.4631(360)	0.0113(300)
	a=3.998(1)Å, b=3.942(3)Å, c=3.999(5)Å,				a=4.028(14)Å, b=3.980(14)Å, c=3.942(15)Å,			
	β=90.332(1)				β= 91.363(139)			
	V=63.037(2)Å^3				V=63.178(22)Å^3			
	Agreement factors: R_{wp}=8.54, R_{exp}=3.26, χ^2=6.83				Agreement factors: R_w=10.37%			

in agreement with an earlier work [56] on KNN50. For the refinements with monoclinic structure with Pm space group, we find that isotropic thermal parameters give satisfactory fits. The Rietveld fitted profiles are shown in Fig. 3.3 with insets showing the fitted profiles of main perovskite reflections {200}, {220}, and {222}. The asymmetric unit of KNN50 at room temperature (Space Group: *Pm*) has five atoms *viz.*, K/Na, Nb, O1, O2, and O3 associated with 1a $(0 \pm u, 0, 0 \pm w)$, 1b $(0.5 \pm u, 0.5, 0.5 \pm w)$, 1a $(0.5 \pm u, 0, 0.5 \pm w)$, 1b $(0 \pm u, 0.5, 0.5 \pm w)$, and 1b $(0.5 \pm u, 0.5, 0 \pm w)$ Wyckoff sites respectively where u and w are refinable parameters. The excellent fits between observed and calculated profiles confirm the correctness of the monoclinic model at long ranges (M_{LRO}). Further, agreement factors namely, R_{wp}, R_{exp}, and χ^2 are within range, which signifies the fit to be good and thus obtained parameters to be reliable.

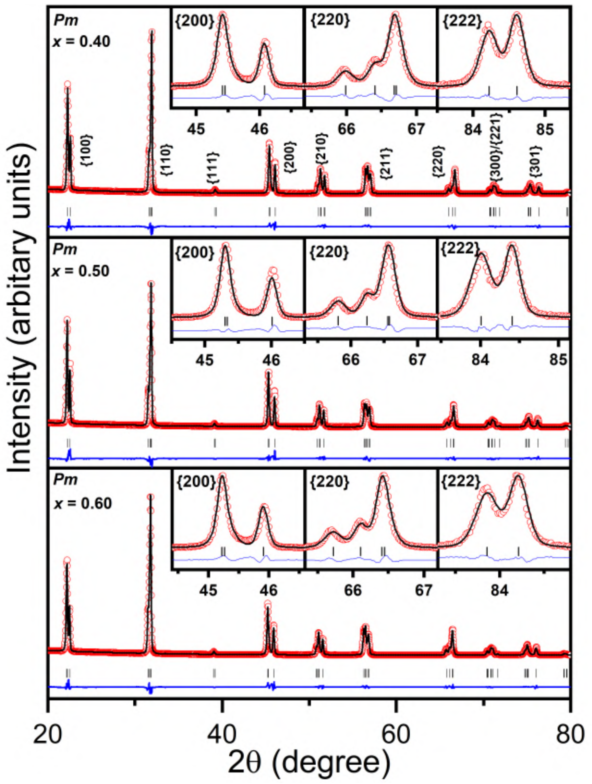

Fig. 3.3 Rietveld Analysis of KNNx (x = 0.40, 0.50, and 0.60) ceramics with insets showing the fits of {200}, {220}, and {222} peaks. The continuous black line represents the simulated patterns while the open red circles represents the observed pattern. The Bragg reflections are represented by vertical black bars, and the continuous blue line at the bottom represents the difference between observed and simulated patterns.

The lattice parameters obtained after Rietveld refinements of HR-XRD data for KNNx are shown in Fig. 3.4. The volume shows a linearly increasing trend with increasing potassium content (x) at A-site, verifying Vegard's law [240]. An anomaly is observed in the monoclinic angle (β) at $x = 0.50$ (KNN50) (see left inset of Fig. 3.4), suggesting maximum monoclinic distortion at $x = 0.50$. This anomalous behavior is further explained in the coming sections.

3.3.2 Raman Analysis of KNNx ceramics

Figure 3.5 depicts the Raman spectra of KNNx ceramics with a bottom figure depicting the evolution of the intensity of prominent Raman peaks (ν_1 and ν_5) as a function of

Table 3.3 Various structural parameters, and agreement factors obtained from the Rietveld (LRO) and PDF (SRO) refinements of the X-ray diffraction patterns and PDF profile for x =0.60 *via* monoclinic (*Pm*) model at LRO and SRO respectively.

Rietveld Refinement					PDF Refinement			
Space group: *Pm*					Space group: *Pm*			
Atoms	x	y	z	B_{iso}(Å^2)	x	y	z	U_{equiv}(Å^2)
K/Na	0.0749(41)	0.0000	0.0649(46)	0.8920(37)	0.9645(91)	0.0000	0.0298(210)	0.0073(11)
Nb	0.5619(16)	0.5000	0.5794(20)	0.1919(14)	0.4702(81)	0.5000	0.5089(130)	0.0045(20)
O_1	0.6008(30)	0.5000	0.0569(41)	0.3948(327)	0.4831(360)	0.5000	0.0367(250)	0.0227(156)
O_2	0.0662(70)	0.5000	0.5621(69)	0.5527(294)	0.0300(300)	0.5000	0.4774(370)	0.0164(170)
O_3	0.6169(30)	0.0000	0.5517(40)	0.0316(112)	0.5920(132)	0.0000	0.4937(141)	0.0239(250)
a=4.007(7)Å, b=3.951(4)Å, c=4.003(1)Å,					a=4.055(14)Å, b=3.930(15)Å, c=3.988(14)Å,			
β=90.299(1)					β= 90.973(140)			
V=63.382(2)Å^3					V=63.544(24)Å^3			
Agreement factors: R_{wp}=8.01, R_{exp}=3.27, χ^2=6.01					Agreement factors: R_w=12.24%			

composition (x). Various Raman bands (or peaks) are observed near 224 cm^{-1} (ν_6), 260 cm^{-1} (ν_5), 545 cm^{-1} (ν_2), 610 cm^{-1} (ν_1), and 850 cm^{-1} ($\nu_1 + \nu_5$). The Raman spectra of all the compositions exhibit analogous peaks and bear a resemblance to the Raman profile for KNN50 ceramics reported in the literature [7, 168, 241]. Rafiq *et al.* compared the experimentally obtained polarized Raman spectrum of KNN50 with orthorhombic (Space Group: *Amm*2) and monoclinic (Space Group: *Pm*) symmetries and found the symmetry to be monoclinic (Space Group: *Pm*) [168].

Generally, the symmetry at intermediate/short ranges at ambient conditions often corresponds to the symmetry of the low-temperature phase observed at long ranges (in case the symmetries at long and short ranges are different in a material) [27, 56, 206, 242, 243]. It is known that Raman scattering can probe the atomic structure comprising of a few tens of unit cells (intermediate/short-range structure), whereas X-ray diffraction provides an average/long-range structure comprising of a few hundred unit cells [244]. Here, for KNNx ceramics, the long-range structure (or average structure) is confirmed to be monoclinic (Space Group: *Pm*) by analyzing HR-XRD data (peak profile analysis and Rietveld refinements). Moreover, the monoclinic phase (Space Group: *Pm*) is also found to be stable at low temperatures for KNN50 [56]. Thus, owing to the above discussion, it is scientifically reasonable to believe that the structure at intermediate/short ranges for KNNx ceramics is monoclinic (which is also the low-temperature phase of KNN50

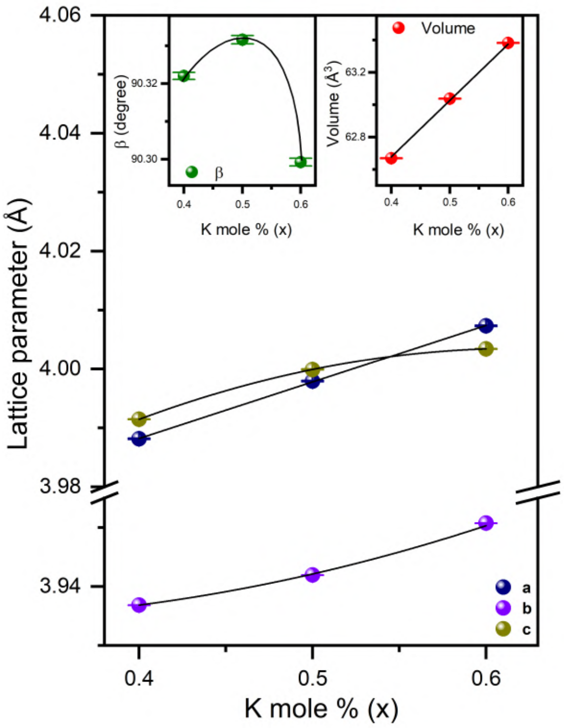

Fig. 3.4 Evolution of lattice parameters (a, b, and c) with left inset showing the anomaly observed in β parameter and right inset showing the volume of LRO structures of KNNx (x = 0.40, 0.50, and 0.60) ceramics.

observed at long ranges). Hence, we conclude from the Raman spectra that KNNx ceramics demonstrate monoclinic symmetry. Further, we have calculated the intensity of the prominent Raman peaks (ν_1 and ν_5) as a function of composition (x). The peak intensity describes the polarizability, presence of the polar phase, etc [7, 202]. Here, it is clearly evident from Fig. 3.5 that the maximum intensity for both the Raman peaks is observed at $x = 0.50$ (KNN50), which is attributed to the high ferroelectric (or polar) content observed for KNN50. Thus, the presence of the maximum amount of polar phase at $x = 0.50$ can be attributed to the high ferroelectric behavior observed for KNN50. Furthermore, the origin of high ferroelectric (or polar) content is explained in the upcoming sections.

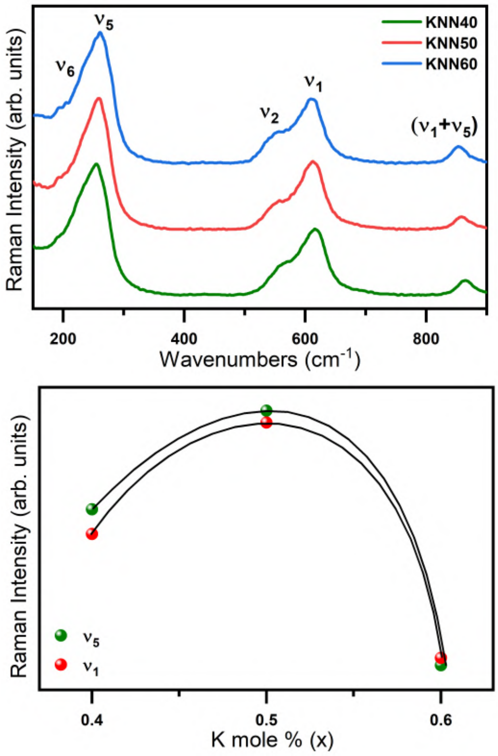

Fig. 3.5 The top figure represents the Raman spectra of KNNx ceramics and the bottom figure represents the Raman intensity of ν_1 and ν_5 peaks.

3.3.3 Short Range Order in KNNx

The process of determining the short range ordering involves the total scattering structure function $S(Q)$ encompassing all the scattering contributions including sharp Bragg peaks, elastic diffuse scattering, and inelastic scattering representing the long range structure, short range structure, and atom dynamics respectively [209]. The observed pair distribution function (PDF) data $G(r)$ is obtained *via* Fourier transformation of high energy synchrotron X-ray diffraction data. The PDF profiles obtained for various KNNx compositions ($x = 0.40$, 0.50, and 0.60) are shown in Fig. 3.6. Further, the property of the Fourier transformation leads to the buildup of experimental errors in the proximity of the origin, specifically at low values of the real space vector r [206]. This phenomenon presents a challenge for structure modeling and refinement processes, as these methods do not account for the effects of experimental errors. As a result, fits of the PDF data for structural features at small r values (*e.g.* approx. less than 2) are rarely of quality [206].

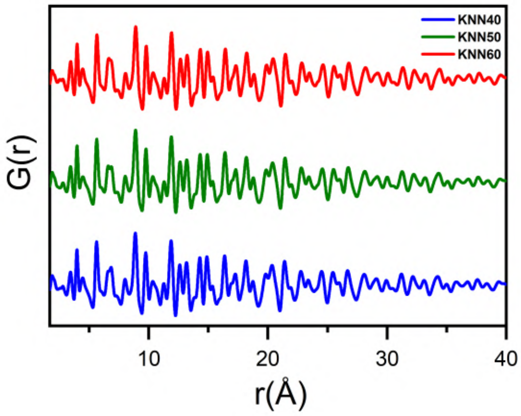

Fig. 3.6 Observed PDF profile of KNNx (x =0.40, 0.50, and 0.60) ceramics for $1.7 \leq r \leq 40$.

Owing to the literature reporting two different atomic orderings for KNN50 (orthorhombic [55, 115, 167, 170] or monoclinic [56, 115]), we have investigated the pair distribution function data thoroughly using partial PDF simulations for monoclinic (*Pm*) and orthorhombic (*Amm*2) space group. The observed peak profiles corresponding to Nb-O and A-O (A = K/Na) bond lengths exhibit relatively broader peaks for the monoclinic space group (*Pm*). This is due to the presence of five and eight unique bond lengths corresponding to Nb-O (Nb-O1×2, Nb-O2×1, Nb-O2×1, Nb-O3×1, and Nb-O3×1) and A-O (A-O1×2, A-O1×2, A-O2×2, A-O2×2, A-O3×1, A-O3×1, A-O3×1, and A-O3×1) bond lengths respectively. In contrast, the orthorhombic space group (*Amm*2) exhibits relatively narrower peaks, attributed to three and five unique bond lengths corresponding to Nb-O (Nb-O1×2, Nb-O2×2, and Nb-O2×2) and A-O (A-O1×2, A-O1×1, A-O1×1, A-O2×4, and A-O2×4) bond lengths respectively. This difference in peak profiles suggests the monoclinic symmetry (space group *Pm*) for our system. The convolution of five and eight peaks related to Nb-O and A-O bonds, aligning with monoclinic symmetry, demonstrates a better fit than the convolution of three and five peaks corresponding to orthorhombic

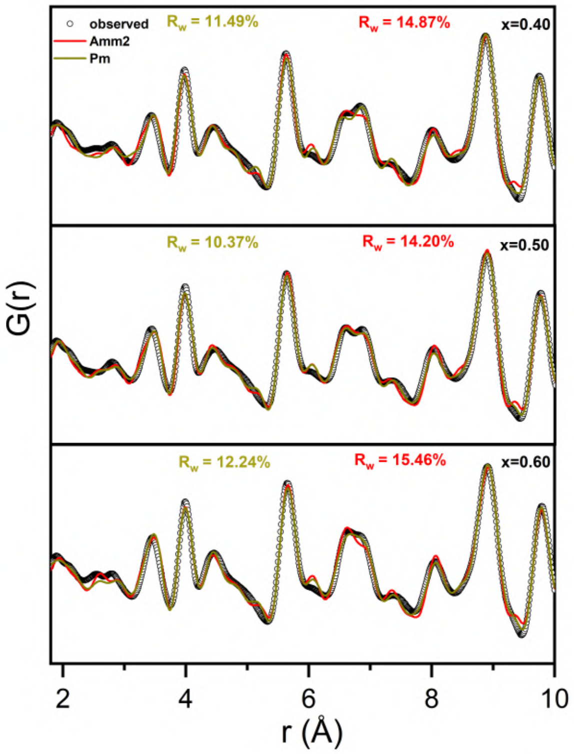

Fig. 3.7 Observed and fitted PDF profile of KNNx (x = 0.40, 0.50, and 0.60) ceramics for $r \leq 10$Å where the black pattern represents the observed data, yellow fit represents the monoclinic (*Pm*) phase, and red fit represents the orthorhombic (*Amm*2) phase.

symmetry. Similar monoclinic symmetry has also been reported by Gupta *et al.* [171] and Kong *et al.* [56] for short-ranges using PDF refinements. Thus, observed PDF profiles of KNNx ceramics were fitted *via* PDFGUI software [213] using the monoclinic (*Pm*) and orthorhombic model (*Amm*2) model (see Fig. 3.7) with initial parameters taken from reported literature [55, 56]. The best fit was obtained for monoclinic (*Pm*) model for all the compositions. Thereafter, lower R$_w$ value (mentioned in the Fig. 3.7) in conjunction with existing literature [56, 171] ascertains the monoclinic symmetry at short-ranges (M_{SRO}). The structural parameters namely lattice parameters, atomic coordinates, isotropic thermal parameters, and volume obtained after refining PDF data has been mentioned in the tables alongside with the Rietveld data (see Tables 3.1, 3.2, and 3.3).

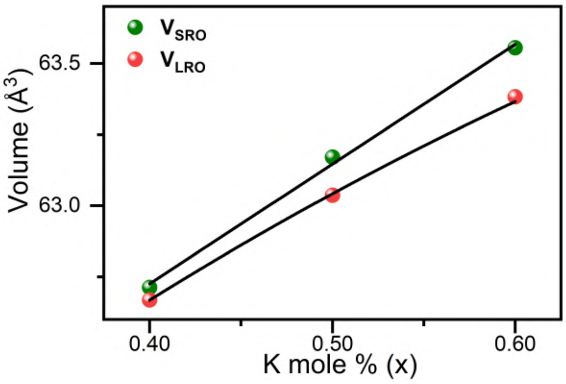

Fig. 3.8 Unit cell volume at long and short ranges for KNNx (x =0.40, 0.50, and 0.60) ceramics.

Further, the volume of the unit cell corresponding to short-range order is found to be greater than the volume of the unit cell at long-range order (see Fig. 3.8), which is analogous to the nanosized effects. This trend is consistent with the observations on other ABO_3-type materials [245, 246]. Moreover, an anomaly in the monoclinic angle (β) is observed at short ranges, similar to long ranges (see Fig. 3.9), maximizing at KNN50 for both long and short ranges. Thus, the monoclinic angle (β) corresponding to long-range structure of KNNx compositions peaks for KNN50, and is attributed to the high monoclinic distortion observed at short ranges. This is similar to what has been observed for $BaTiO_3$ based solid solutions, where the local rhombohedral structure drastically influences the macroscopic properties of the material [142, 206]. Further, the difference in the monoclinic angle (β) between long and short ranges is plotted as a function of composition (x) (see the inset of Fig. 3.9) representing the *degree of uniqueness* corresponding to the two monoclinic phases (M_{LRO} and M_{SRO}). Moreover, the contribution of M_{SRO} in the macroscopic properties has been attributed to the degree of uniqueness. Thus, the maximization of ferroelectric properties for KNN50 is attributed to the maxima observed in the degree of uniqueness for $x = 0.50$.

Further, the origin of the anomaly in the monoclinic angle (β) for long and short ranges is explained using another parameter *viz.*, separation parameter (δd) which is defined as the difference between the d-spacing of the two peaks linked with the two sets of distinct planes observed in the diffraction pattern of the monoclinic phase corresponding to the 8 equivalent planes of {hhh} family of a cubic crystal system. It is important to note that the d-spacing (d_{hkl}, d'_{hkl}) and its difference ($\delta d = d_{\mathrm{hkl}} - d'_{\mathrm{hkl}}$) corresponding to {hhh} type reflections of a cubic crystal system is characterised by the variable coordinates (a, b, c, and β) of the monoclinic crystal system. Here, we see that planes corresponding to {hhh} family involve equal weightage along the three crystallographic axes and can be considered as an important order parameter to quantify the monoclinic distortions. Now, $d_{\{\mathrm{hkl}\}}$ corresponds to the set of planes *viz.*, (111), $(1\bar{1}1)$, $(\bar{1}1\bar{1})$, and $(\bar{1}\bar{1}\bar{1})$, and $d'_{\{\mathrm{hkl}\}}$ corresponds to the set of planes *viz.*, $(\bar{1}11)$, $(11\bar{1})$, $(\bar{1}\bar{1}1)$, and $(1\bar{1}\bar{1})$. The d-spacing for the two distinct set of planes ($d_{\{\mathrm{hkl}\}}$ and $d'_{\{\mathrm{hkl}\}}$) for a monoclinic crystal system is given by [185]:

$$\frac{1}{d^2{}_{\{\mathrm{hkl}\}}} = \frac{1}{sin^2\beta}\left(\frac{h^2}{a^2} + \frac{k^2 sin^2\beta}{b^2} + \frac{l^2}{c^2} - \frac{2hl cos\beta}{ac}\right) \tag{3.9}$$

$$\frac{1}{d'^2{}_{\{\mathrm{hkl}\}}} = \frac{1}{sin^2\beta}\left(\frac{h^2}{a^2} + \frac{k^2 sin^2\beta}{b^2} + \frac{l^2}{c^2} + \frac{2hl cos\beta}{ac}\right) \tag{3.10}$$

The separation parameter (δd) dictates the magnitude of β for monoclinic phase *i.e.*, larger the separation δd, greater is the magnitude of β. The separation δd has been calculated at long and short ranges (see Fig. 3.10) with the difference of δd between long and short ranges is shown in the inset of Fig. 3.10. The separation parameter is maximum for KNN50 consistent with the nature of the monoclinic angle (β) corresponding to the monoclinic phases (M_{LRO} and M_{SRO}). Further, the difference in δd between M_{LRO} and M_{SRO} given as $D = (\delta d_{\mathrm{SRO}} - \delta d_{\mathrm{LRO}})$ (see inset of Fig. 3.10) suggests unique behavior of M_{SRO} imparting its maximum influence (or peaking) at $x = 0.50$.

Now, from basic crystal-chemical arguments, one would expect the substitution of the larger K^{1+} (164 pm) cations by smaller Na^{1+} (139 pm) cations and the associated

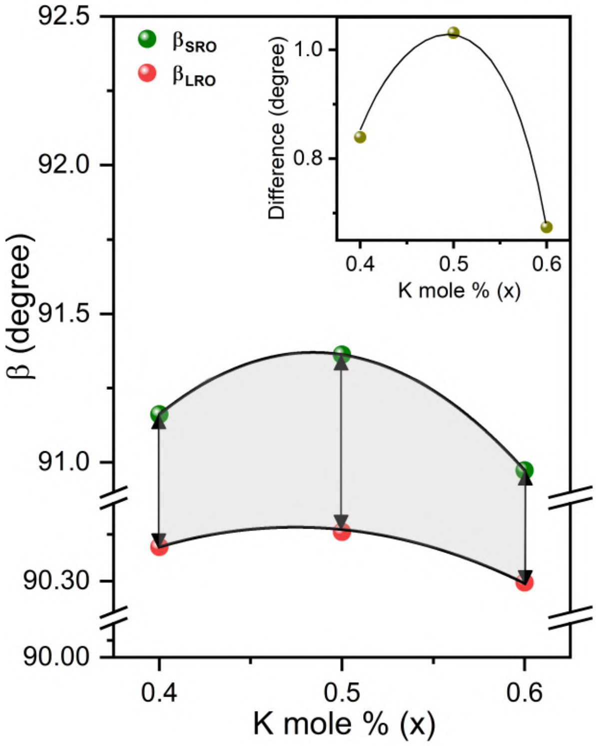

Fig. 3.9 Monoclinic angle β at LRO and SRO of KNNx (x = 0.40, 0.50, and 0.60) ceramics with inset showing the difference in the monoclinic angle at LRO and SRO.

changes at the local and nanoscale structure to be significant for the distortions and ferroelectric properties in this system [148, 238]. Thus, the presence of unique monoclinic phase (M_{SRO}) at short ranges is attributed to the ionic radii mismatch between K^{1+} and Na^{1+} cations. The distortion resulting from the ionic radii mismatch is maximum at x = 0.50 (observed in various structural parameters) leading to better physical properties *viz.*, dielectric permittivity, piezoelectric coefficient, remnant polarization, and many more widely reported in literature for KNN50 [108, 115, 184, 238, 247, 248, 249, 250, 251]. Further, frozen phonon mode approach has been used to establish structure-property relationship *via* quantification of ferroelectric distortions (or polarization) observed at short- and long-ranges.

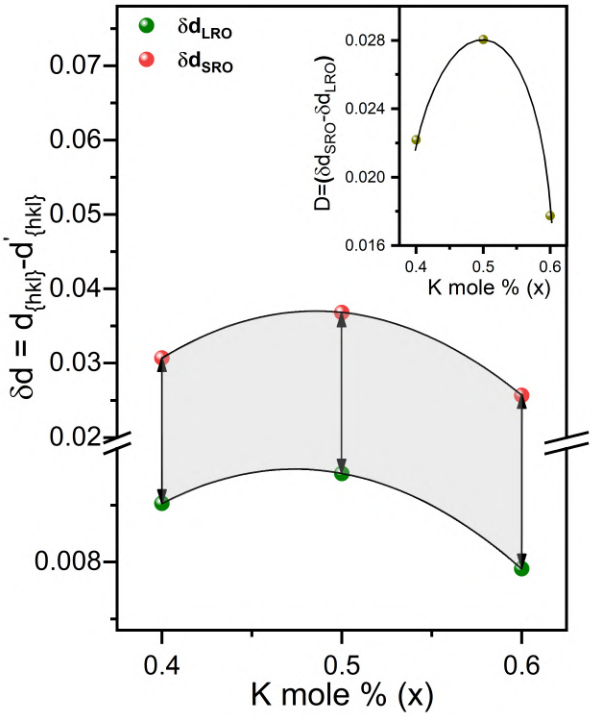

Fig. 3.10 The separation parameter (δd) plotted against the increasing potassium content (x) for SRO and LRO with inset showing the difference of the separation (δd) between SRO and LRO given as D=($\delta d_{\mathrm{SRO}} - \delta d_{\mathrm{LRO}}$) for KNNx ceramics.

3.3.4 Frozen phonon mode of KNNx

The variations in lattice parameters and atomic coordinates of various atoms are held responsible for distortions in the unit cell which may lead to non analytical behavior at structural phase transitions [227]. The distortion based study in accordance with atomic displacements at various length scales gives us a deep insight of the overall structure. Further, in order to quantify the ferroelectric distortions leading to structural phase transition(s) frozen (condensed) phonon mode approach is taken into consideration. The structural phase transitions are outcome of small atomic displacements resulting due to condensation of soft phonon modes (*i.e.*, the normal mode of vibrations in the lattice) [232, 252, 253]. Further, the transition to a low symmetry distorted structure from a high symmetry undistorted structure is attributed to the condensation of one or more soft phonon modes, which can be viewed as correlated vibrations of atoms corresponding to the high symmetry cubic phase. Here, the high symmetry cubic phase (*Pm*$\bar{3}$*m*) is taken as reference structure with lattice parameter a = 3.98703 Å and A-site, B-site, and Oxygen atoms are fixed at 1b (0.5, 0.5, 0.5), 1a (0, 0, 0), and 3d (0.5, 0, 0) Wyckoff positions respectively. The phonon mode(s) responsible for symmetry breaking is referred as primary while other mode(s) are referred as secondary. In the frozen phonon mode analysis, the order parameter (primary or secondary) can be described as a vector that is located in the distortion space and is aligned with a specific order parameter direction (OPD) within an irreducible representation (irrep) at a particular point in the reciprocal space [236]. Further, a group-subgroup relation always exists between high symmetry and low symmetry structures given by:

$$r(\mu,i) = r_0(\mu,i) + u(\mu,i) \tag{3.11}$$

where, $r(\mu,i)$ is the position of μ (μ=1,2,3,4,....) atom corresponding to the low symmetry space group, $r_0(\mu,i)$ corresponds to atomic positions of high symmetry space group, and $u(\mu,i)$ is the static atomic displacements present in low symmetry structure [236, 253]. In order to analyze and quantify the distortions of the low symmetry unit cell, we have used AMPLIMODES package available at Bilbao Crystallographic Server [232, 233, 234, 235]. The lattice parameters, atomic coordinates, and site multiplicity of low symmetry and high symmetry structures are used as inputs to carry out phonon modes decomposition.

As discussed above we have confirmed a monoclinic phase with *Pm* space group at long and short ranges for KNN*x* (x = 0.40, 0.50, and 0.60) ceramics. This monoclinic phase results from the freezing of triply degenerate ferroelectric phonon mode (Γ_4^-) corresponding to the zone centre of cubic Brillouin zone. Here, the component freezing of Γ_4^-, along the two dimensions with unequal magnitudes lead to order parameter direction $(b,0,a)$, resulting into a low symmetry monoclinic phase *Pm* (see Fig. 3.11(a)). In addition to Γ_4^- phonon mode acting as primary order parameter, a non-polar antiferroelectric phonon mode

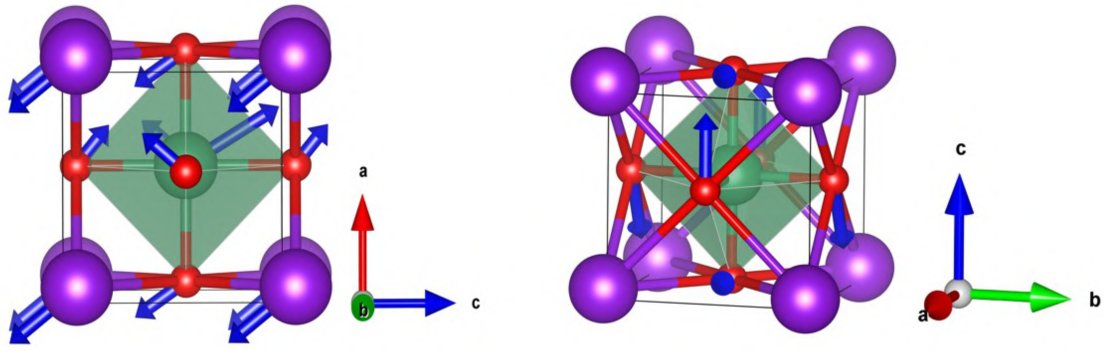

(a) Γ_4^- (b,0,a)

(b) Γ_5^- (a,b,0)

Fig. 3.11 The description of (a) Γ_4^- and (b) Γ_5^- phonon modes with OPD. The A-site atoms (purple) are at corner, B-site atom (green) at body center, and oxygen atoms (red) are at face center. The arrows represents the direction of atoms displacement. The figures were obtained from VESTA software [16].

[191, 212] *viz.*, Γ_5^- acting as a secondary order parameter is also observed in a monoclinic phase (see Fig. 3.11(b)). The 1b and 1a site of high symmetry cubic phase transforms into 1a and 1b site of low symmetry monoclininc phase *via* Γ_4^- phonon mode. There are two Γ_4^- phonon modes associated with each A and B-site atoms mentioned in Table 3.4. On the other hand, 3d site of high symmetry phase corresponding to oxygen atoms splits into 1b, 1b, and 1a site *via* condensation of four Γ_4^- and two Γ_5^- phonon modes. Thus, freezing of total eight Γ_4^- and two Γ_5^- phonon modes results in low symmetry monoclinic phase having ten variable coordinates (see Table 3.4).

Table 3.4 Frozen phonon modes for low symmetry distorted structure (*Pm*).

Atom	Wyckoff site ($Pm\bar{3}m$)	Wyckoff site (*Pm*)	Irrep(s)
A (K/Na)	1b (0.5,0.5,0.5)	1a (x,0,z)	Γ_4^-(2)
B (Nb)	1a (0,0,0)	1b (x,0.5,z)	Γ_4^-(2)
O	3d (0.5,0,0)	1b (x,0.5,z) 1b (x,0.5,z) 1a (x,0,z)	Γ_4^-(4) and Γ_5^-(2)

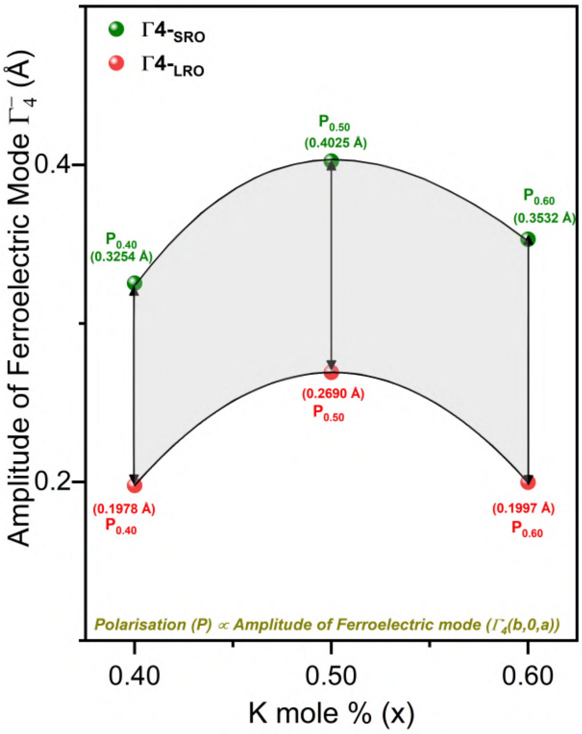

Fig. 3.12 Mode amplitude of KNN*x* (*x* = 0.40, 0.50, and 0.60) ceramics at LRO and SRO with red color representing the LRO structures while green color representing SRO structures.

Table 3.5 Amplitude of the phonon mode(s) in low symmetry ferroelectric phase (monoclinic, *Pm*) of KNN*x* (0.40, 0.50, and 0.60) ceramics, with respect to high symmetry cubic ($Pm\bar{3}m$) phase.

Composition (*x*)	Phase	Irrep	OPD	Amplitude (Å)	
				LRO	SRO
0.40	*Pm*	Γ_4^-	(b,0,a)	0.1978	0.3254
		Γ_5^-	(a,b,0)	0.0437	0.3184
0.50	*Pm*	Γ_4^-	(b,0,a)	0.2690	0.4025
		Γ_5^-	(a,b,0)	0.0451	0.2125
0.60	*Pm*	Γ_4^-	(b,0,a)	0.1997	0.3532
		Γ_5^-	(a,b,0)	0.0540	0.3103

The freezing of the Γ_4^- phonon modes leads to ferroelectric displacements which are quantified by the amplitude of the ferroelectric phonon mode (Γ_4^-). These ferroelectric displacements directly corresponds to the microscopic dipole moments of the unit cell which consequently leads to macroscopic polarization of the system.

The calculated amplitudes of the ferroelectric phonon mode (Γ_4^-) and the antiferroelectric phonon mode (Γ_5^-) corresponding to the unit cells at long and short ranges are given in Table 3.5. The amplitude of Γ_4^- phonon mode is significantly higher at short ranges in comparison to long ranges ($\approx$ 150 % - 180 %), and peaks at KNN50 (see Fig. 3.12). Here, it is important to note that the maximization at $x = 0.50$ in structural and ferroelectric distortion parameters *viz.*, the amplitude of the ferroelectric phonon mode (Γ_4^-) (long and short ranges), intensity of prominent Raman peaks, and relatively high degree of monoclinic distortion (β and δd) arise from ionic radii mismatch between K^{1+} and Na^{1+} cations causing high distortions at long- and short-ranges which further contributes to the macroscopic properties. Various physical properties such as dielectric permittivity ($\varepsilon \approx$ 410-571 [247, 248, 254]), piezoelectric coefficient ($d_{33} \approx$ 120-160 pC/N [115, 247, 248, 254]), remnant polarization ($P_r = 31.5\ C/cm^2$ [115]), electromechanical coupling coefficient ($k_t \approx$ 0.47 [115]), and many more peaks at $x = 0.50$ [108, 115, 184, 247, 248, 249, 250, 251, 254]. The maxima in the ferroelectric properties for KNN50 is the consequence of significantly high amplitude of ferroelectric phonon mode (Γ_4^-) observed at long and short ranges along with maximum intensity observed in prominent Raman peaks. Moreover, the high ferroelectric responses observed at $x = 0.50$ are attributed to the presence of two uniquely distinct monoclinic phases (M_{LRO} and M_{SRO}) with maximum distortions observed at MPB composition. Hence, it is reasonable to believe that the monoclinic phase at short range order (M_{SRO}) with relatively high ferroelectric polarization (Γ_4^-) in comparison to monoclinic phase at long-range order (M_{LRO}), collectively tunes the ferroelectric properties of the material (KNNx) in a correlated fashion [142, 206].

3.4 Conclusion

In conclusion, the structural analysis at various length scales (long/short ranges) in an MPB composition *viz.*, KNN50 and its vicinity reveal a monoclinic phase (Space Group:

Pm), which contrasts a very recent report by Saha *et al.* [167]. Moreover, the dominance of ferroic order parameter *viz.*, ferroelectric polarization (amplitude of Γ_4^-) for KNNx ceramics (x = 0.40, 0.50, and 0.60) at short-ranges over long-ranges has been quantified for the very first time. It is clearly evident from the study that high physical properties *viz.*, dielectric constant, piezoelectric coefficient, remnant polarization, electromechanical coupling coefficient etc. The MPB composition reported for KNNx *i.e.*, KNN50 is attributed to the two unique monoclinic phases (M_{LRO} and M_{SRO}) characterized by the degree of uniqueness. The amplitude of the ferroelectric distortion mode (Γ_4^-) for M_{SRO} is significantly higher than that of M_{LRO} and both peaks at x = 0.50. Moreover, the intensity of prominent Raman peaks (ν_1 and ν_5) maximize at x = 0.50, depicting the increase in ferroelectric (or polar) content. Further, the largest difference in the monoclinic distortion parameters (β and δd) for M_{LRO} and M_{SRO} can also be correlated to the maxima in the ferroelectric properties reported for KNN50. Thus, the ferroelectric properties of KNNx (0.40, 0.50, and 0.60) have been attributed to the two uniquely distinct monoclinic phases (M_{LRO} and M_{SRO}) which are collaboratively held responsible for the enhancement of the ferroelectric properties for KNNx ceramics with a maxima at KNN50. Overall, a structure-property correlation is established by blending the ferroelectric properties observed at short- and long-ranges for widely reported MPB composition *i.e.*, KNN50.

In the next chapter, we will discuss the structure-property correlations in a KNN50-based solid solution and will explain the emergence of long-range ferroelectric order from short ranges.